PHYSICAL REVIEW B VOLUME 51, NUMBER 6 1 FEBRUARY 1995-II

Valence electronic structure of polycrystalline SiC as observed by $(e,2e)$ spectroscopy

Y. Q. Cai, M. Vos, P. Storer, A. S. Kheifets, I. E. McCarthy, and E. Weigold*
Electronic Structure of Materials Centre, The Flinders University of South Australia,
GPO Box 2100, Adelaide, S.A. 5001, Australia

(Received 27 July 1994; revised manuscript received 18 October 1994)

The spectral momentum density $\rho(\epsilon,q)$ of the valence electrons of a thin polycrystalline silicon carbide (SiC) film has been measured using an $(e,2e)$ spectrometer employing a noncoplanar asymmetric geometry with estimated energy and momentum resolutions of about 2.0 eV and 0.15 a.u., respectively. Well-defined valence-band dispersion has been observed from the measured momentum density which resembles a parabola, but deviates from what is expected for a free electron near the top of the band and at the boundary of the Brillouin zone, where the antisymmetric gap due to the unequal potentials between the Si and C sites in SiC is clearly visible. Based on the assumption that the spectral momentum density of polycrystalline materials is a spherical average of the spectral momentum density of the corresponding single crystalline phase of the materials, *ab initio* linear muffin-tin orbital calculations have been performed using the zinc-blende structure of β-SiC. The measured dispersion of the energy band is in excellent agreement with theory. Reasonable agreement is also obtained for the energy-integrated momentum density, although the measured momentum density exceeds considerably the calculated one at high momenta. The theoretical implication of using crystal band-structure calculations for studying disordered materials is also discussed.

I. INTRODUCTION

Electron-coincidence experiments, in which an incoming electron knocks out a bound electron in a collision and the two outgoing electrons are then detected in time coincidence with defined kinematics, are known as $(e,2e)$ experiments. This type of experiment has been applied with great success to the study of the momentum distribution of the valence electrons of atoms and molecules in the gas phase.[1] The main reasons behind this success are the ability of the $(e,2e)$ reaction to probe the motion (the energy and the real momentum) of the electrons of a system and the proportionality of the $(e,2e)$ differential cross section to the spectral momentum density $\rho(\epsilon,\mathbf{q})$ of the system under the conditions of high energy and momentum transfer. In fact, for each clean knockout, if the energy and momentum of the incident electron are E_0 and $\mathbf{p}_0$, respectively, by measuring the energy and momentum of the scattered (E_s, $\mathbf{p}_s$) and the ejected (E_e, $\mathbf{p}_e$) electrons, the precollision binding energy and momentum of the ejected electron (ϵ, $\mathbf{q}$) can be obtained using the energy and momentum conservation laws[1]

$$\epsilon = E_0 - E_s - E_e, \tag{1}$$

$$\mathbf{q} = \mathbf{p}_s + \mathbf{p}_e - \mathbf{p}_0. \tag{2}$$

Note that at sufficiently high incident energy and momentum transfer, it is assumed that the precollision electron momentum $\mathbf{q}$ is equal and opposite to the observed recoil momentum $\mathbf{p}_0 - \mathbf{p}_s - \mathbf{p}_e$. This assumption is experimentally verifiable. It is true if apparent structure information such as the momentum density is independent of the incident energy. Experience with gaseous systems[1] has verified that the present kinematic conditions are more than adequate for the assumption to be valid as far as the momenta of probe electrons near the collision point are concerned.

In the case of solids, the $(e,2e)$ differential cross section can also be shown to be proportional to the spectral momentum density $\rho(\epsilon,\mathbf{q})$ of the valence electrons under the plane-wave impulse approximation.[2] The effect of further scattering of the probe electrons before and/or after the collision at other points in the solid must be taken into account by a deconvolution procedure based on the results of an electron scattering experiment.[3] For over 20 years, however, there have been only a few reports on $(e,2e)$ studies of solid materials due to the experimental difficulties involved, and the results were shadowed by the poor energy resolutions and excessively long data acquisition time.[4–7] With the construction of an $(e,2e)$ spectrometer utilizing parallel detection technology and a noncoplanar asymmetric geometry,[8] these problems have largely been overcome. The $(e,2e)$ technique has begun to show its potential as a powerful tool for studying the valence electronic structure of solid materials in the form of free-standing films. A series of experiments have been performed recently using this spectrometer on materials such as highly oriented pyrolitic graphite (HOPG),[9] amorphous carbon,[10] evaporated silicon,[11] and silicon carbide, with energy resolution of around 2.0 eV, momentum resolution of around 0.15 a.u. [1 atomic unit (a.u.) $= a_0^{-1} = 1.89$ Å^{-1}], and good statistics of coincidence counts for each measurement being obtained over a period of 4–5 days. With proper deconvolution of the measured intensity that is primarily due to multiple scattering effects,[3] the electron distribution in energy and momentum space [i.e., the spectral momentum density $\rho(\epsilon,\mathbf{q})$] of these materials can be imaged directly. In the present paper, this imaging power of the $(e,2e)$ technique will be highlighted using data taken from amorphous carbon, evaporated silicon, and a polycrystalline phase of silicon carbide. The images of the three momentum densities show not only well-defined energy band dispersion, but also distinctive features that are clearly associated with the local order of the materials. The relation between the three spectral momentum densities is found to be well described by the one-electron-band theory of crystalline solids. It is also found that crystal band-structure calculations plus a spherical average of the calculated momentum density describe well these disordered materials, and will be discussed in association with the details of the SiC results. The theoretical implication of using crystal band-structure calculations for studying disordered materials is also discussed.

The rest of this paper is organized as follows: The theoretical aspects for the calculation of the momentum density of SiC is discussed first in Sec. II, followed by a description of the experimental details in Sec. III. The results and discussion are then given in Sec. IV. Finally the results are summarized in Sec. V.

II. THEORY

Traditionally electronic structures of disordered and amorphous materials are calculated using approaches such as atomic orbital and tight-binding methods that depend only on the local order of the materials.[12] This of course has its logical reasons because in disordered and amorphous materials the long-range order is lost, and one can no longer use, at least not without modifications, methods such as pseudopotentials, orthogonalized plane waves, or muffin-tin potentials that require the presence of periodicity and the validity of Bloch's theorem. With some modifications, however, these two classes of approaches are complementary in describing disordered and amorphous materials,[13,14] and both can come to the same conclusions that band dispersions exist in disordered and amorphous materials and that they are similar to those observed in crystalline materials provided that the disordered and amorphous materials retain a similar local order. This similarity has been verified experimentally in our amorphous silicon data.[11]

Therefore, by extending the approach described in Ref. 14, one can consider an ideal amorphous or disordered solid as comprising atomic clusters of certain size, each cluster having the local order of the corresponding crystal structure and the same periodic boundary conditions. The electronic structure of this ideal amorphous solid is then expected to be represented well by crystal band-structure calculations. A spherical average of the calculation may be performed to simulate the random orientation of these clusters. The more homogeneous this random orientation, the better the simulation would be. As real amorphous solids are often found to retain a similar local order, one can use this method to approximate the electronic structure of amorphous solids and be able to utilize the many existing highly developed crystal band-structure calculation techniques. In our case, we found that this method works well for amorphous silicon[11] and a polycrystalline phase of silicon carbide. Under this method, the only difference between an amorphous state and a polycrystalline state of a solid is the difference in the size of the atomic clusters, which requires no extra treatment.

Silicon carbide is an interesting material in its own right. It has great potential for applications in high-power, high-temperature microelectronic and/or optoelectronic devices.[15] In crystalline form, SiC exits with over 100 different structure variations (called polytypes). The structure of these polytypes can be understood in terms of a hexagonal system, the stacking order along the c axis differing from one polytype to another. One form of these polytypes is cubic (by taking the [111] direction as the "c axis") and is known as β-SiC, exhibiting a zinc-blende structure. Another form has the wurtzite structure with many variations, and is collectively called α-SiC. β-SiC is formed preferentially at temperatures below 2000 °C. Transformation from β-SiC to α-SiC occurs only at temperatures above 2100 °C. In all polytypes every atom is tetrahedrally surrounded by four atoms of the other species. The bonds between silicon and carbon atoms have a nearly covalent character, with an ionic contribution of about 10% (silicon positively, carbon negatively charged).[16]

For experimental reasons (see Sec. III), only the zinc-blende structure of β-SiC is considered here. The first Brillouin zone (face-centred cubic) is shown in Fig. 1, with all the symmetry axes and critical points indicated. The valence-band structure is calculated using the linear muffin-tin orbital (LMTO) method.[17] This is an *ab initio* self-consistent method which has the accuracy and computational efficiency sufficient to perform full-scale band structure calculations. Since we measure real momentum $\mathbf{q}$ in our $(e,2e)$ experiments, and $\mathbf{q} = \mathbf{k} + \mathbf{G}$, where $\mathbf{k}$ is the crystal momentum restricted to the first Brillouin zone and $\mathbf{G}$ is a reciprocal lattice vector, the calculation results along the three major symmetry axes ΓX, $\Gamma K X$, and ΓL, shown in an extended-zone scheme in Fig. 2(a) to reflect the band structure with respect to the real momentum. Under the one-electron approximation

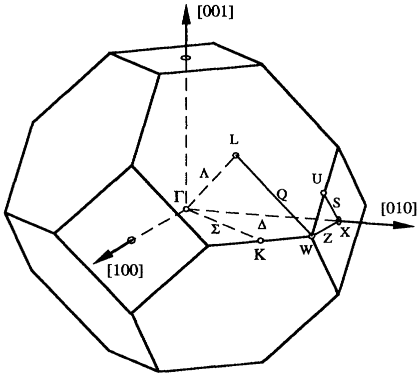

FIG. 1. The first Brillouin zone of a face-centred-cubic (fcc) lattice. All symmetry axes and critical points are indicated.

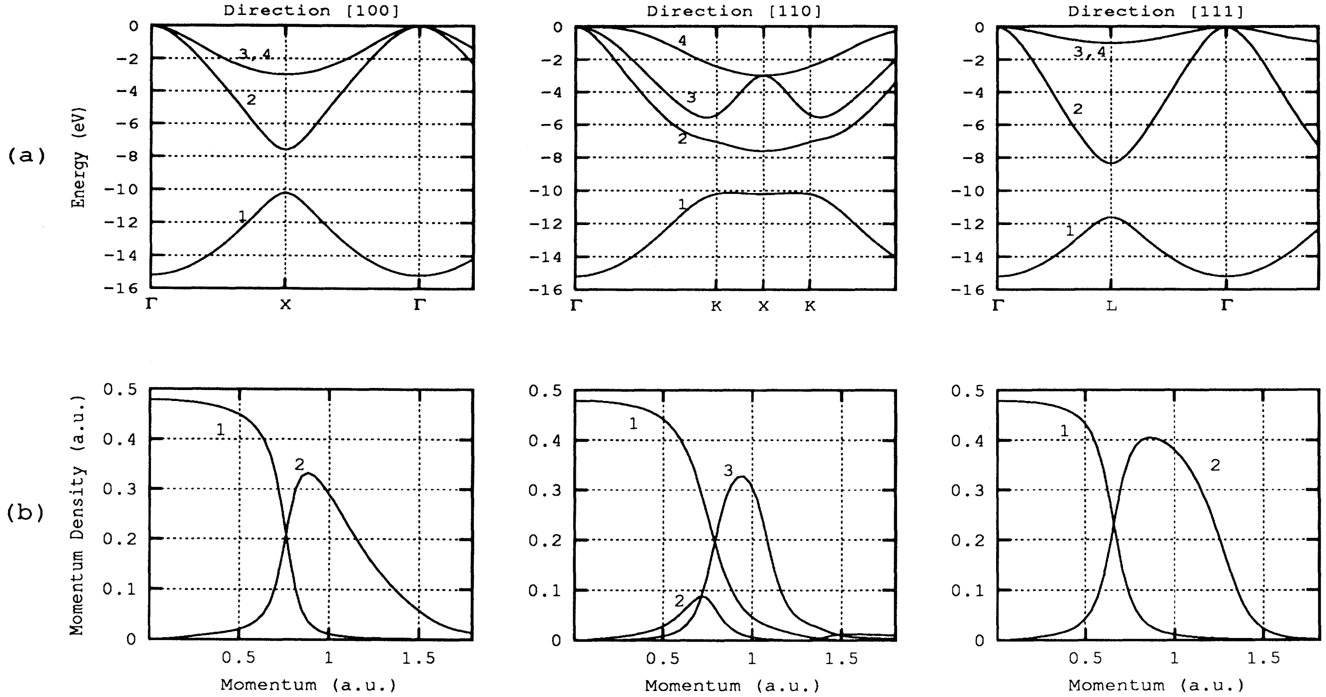

FIG. 2. Energy band structure (a) and momentum density (b) for β-SiC along the three major symmetry axes ΓX, ΓKX, and ΓL, shown in an extended zone scheme, as calculated by the LMTO method.

the combined energy momentum density for each band $\rho_j(\epsilon,\mathbf{q})$ is proportional to the square of the one-electron wave function in momentum space and is calculated from the expression[18]

$$\rho_j(\epsilon,\mathbf{q}) = (2\pi)^{-3}\sum_{\mathbf{Gk}} n_{j\mathbf{k}} \left| \int d^3r\,\psi_{j\mathbf{k}}(\mathbf{r})e^{-i\mathbf{q}\cdot\mathbf{r}}\right|^2 \times\delta(\epsilon - E_{j\mathbf{k}})\delta(\mathbf{q}-\mathbf{k}-\mathbf{G}), \qquad (3)$$

where $n_{j\mathbf{k}}$ is the occupation number of the corresponding one-electron state, and $\psi_{j\mathbf{k}}$ and $E_{j\mathbf{k}}$ are the one-electron wave function and energy defined by the band index j and the crystal wave vector $\mathbf{k}$, respectively. The reciprocal vector $\mathbf{G}$ translates $\mathbf{q}$ to the first Brillouin zone. The wave function $\psi_{j\mathbf{k}}$ is constructed from spherical harmonics,

$$\psi_{j\mathbf{k}}(\mathbf{r}) = \sum_{lm} a^{j\mathbf{k}}_{lm} i^l Y_{lm}(\hat{r})\frac{1}{r}P_l(r), \qquad (4)$$

where $a^{j\mathbf{k}}_{lm}$ are the coefficients for the muffin-tin orbitals and $P_l(r)$ are the radial orbitals normalized to unity over the muffin-tin sphere. Summation over the number of muffin tins should also be included in Eq. (4) if there is more than one nonequivalent atom per elementary cell. The integration in Eq. (3) is carried out over the muffin tin where the wave function $\psi_{j\mathbf{k}}$ is normalized to unity. The spectral momentum density has been normalized over energy and momentum space to the number of valence electrons per unit cell per spin:

$$2\sum_j \int d\epsilon d^3q\rho_j(\epsilon,\mathbf{q}) = 2\sum_j \int d^3q\rho_j(\mathbf{q}) = N_e. \qquad (5)$$

The resulting momentum densities $\rho_j(\mathbf{q})$ for all the bands involved are shown in Fig. 2(b).

From Fig. 2 one can see that, for crystalline β-SiC and along the three major symmetry directions, mainly the electrons from the lower valence band (band 1) contribute to the momentum density within the first Brillouin zone. In the second Brillouin zone and along the ΓX and the ΓL directions, the density for band 2 dominates, whereas the density for band 3 peaks and dominates along the ΓKX direction, being lower along other directions. There is no contribution to the momentum density from electrons occupying band 4 along the three major symmetry directions, but the contribution is expected to exist in other directions with lower symmetry and is included in the spherically averaged momentum density presented in Sec. IV. In all three major symmetry directions, the energy dispersion of the combined density with respect to the real momentum resembles the nearly free electron parabola, but deviates strongly from it near the zone boundary with the opening of the antisymmetry gap, which is caused by the ionicity of the Si-C bond, between the lower band 1 and the upper bands 2, 3, and 4. This basic feature of the energy dispersion remains even after the spherical average as we will see in Sec. IV.

Finally, to obtain the momentum density for the polycrystalline SiC, the momentum density $\rho_j(\epsilon,\mathbf{q})$ of Eq.(3) is averaged spherically:

$$\rho(\epsilon, q) = \sum_j (4\pi)^{-1} \int d\Omega_{\mathbf{q}} \rho_j(\epsilon, \mathbf{q}). \tag{6}$$

For symmetry reasons, the averaging can also be performed over the irreducible wedge of the fcc Brillouin zone. The finite energy and momentum resolutions of the experiment can also be taken into consideration by replacing the energy and momentum δ function in Eq. (3) with a Gaussian of the appropriate width. The final results are presented in Sec. IV when the experimental results are compared with the theory.

III. EXPERIMENT

A detailed description of the $(e, 2e)$ spectrometer has been given in Ref. 8. A noncoplanar asymmetric geometry is used as shown in Fig. 3(a). The asymmetric geometry is chosen because the electron-electron scattering cross section peaks strongly in the forward direction. The energy of the incident electrons is 20 keV but can be scanned up by 100 eV to probe regions further below the vacuum level. The kinematics chosen is such that the scattered (ejected) electron has energies of around 18.8 keV (1.2 keV) and a polar angle of 14° (76°). With this kinematics, the momentum components of the three electrons in the xz plane cancel out, and the momentum of the target electron is detected only along the y axis [Eq. (2)]. A hemispherical and a toroidal analyzer are employed to detect in parallel the scattered and the ejected electrons over a range of azimuthal angles and energies, respectively. The energy and azimuthal angle ranges are $18\,790\text{ eV} \leq E_h \leq 18\,810\text{ eV}$ and $-18^\circ \leq \phi_h \leq 18^\circ$ for the hemisphere analyzer, and $1\,182\text{ eV} \leq E_t \leq 1\,218\text{ eV}$ and $\pi - 6^\circ \leq \phi_t \leq \pi + 6^\circ$ for the toroidal analyzer. $(e, 2e)$ experiments are performed in transmission. The target thin film is held vertically and forms an angle of about 30° towards the incident beam [Fig. 3(b)]. The measured electron momentum is in the film plane. The surface of interest is placed on the exit side. The escape depth of the lower-energy ejected electrons is about 10–20 Å, which determines the surface-sensitive nature of the current experiment.

The target preparation began with evaporated carbon films obtained from Arizona Carbon Foil Co. Films with nominal thickness of 80 Å were used. The films were floated off their glass support in de-ionized water and were transferred onto a molybdenum sample holder with holes of 2 mm in diameter. Before the Si evaporation the carbon films were annealed under vacuum in a preparation chamber for 10 min in order to remove the small amount of oxygen on the surface. This annealing also caused the carbon film to recrystallize in some way.[10] The annealing was performed using electron bombardment of the sample holder generated by a tungsten filament placed about 1 mm away from the films, with a bias voltage of 1 keV between the filament and the holder and a beam current of 2 mA. A Si layer of about 30 Å thickness was then deposited onto the carbon film with an evaporation rate of about 6 Å per hour. The pressure in the chamber was maintained at about 4×10^{-9} torr during the evaporation. Finally, the Si/C film was annealed for 10 min under the same conditions as described above to obtain a polycrystalline phase of SiC. No accurate monitoring of the annealing temperature was available, but it was estimated to be at least 600 °C. Within this temperature range it has been reported that mainly fine-grained polycrystalline β-SiC was formed.[19] Between each step, an $(e, 2e)$ measurement was performed on the sample in a measurement chamber with a base pressure of 2×10^{-10} torr over a period of 4 – 5 days. The overall energy and momentum resolutions were estimated to be 2.0 eV and 0.15 a.u., respectively.

IV. RESULTS AND DISCUSSION

We now return to the presentation and discussion of the results. Figure 4 presents the images of the spectral momentum densities as a function of binding energy and momentum of the three films. An empirical deconvolution procedure has been used to deconvolute the "background" at higher binding energies caused primarily by plasmon excitation by one of the $(e, 2e)$ electrons.[3] The density is given by the linear grey scale, which corresponds to the intensity of the deconvoluted spectra. The energy and momentum axes are chosen with the same ranges to facilitate a direct comparison between the three data sets. From here one can see that the main band structure of the amorphous carbon film [Fig. 4(a)] is quite broad in momentum and deep in energy, the density peaking at $q = 0$ at the bottom of the band. The evaporated silicon [Fig. 4(b)] shows band features much

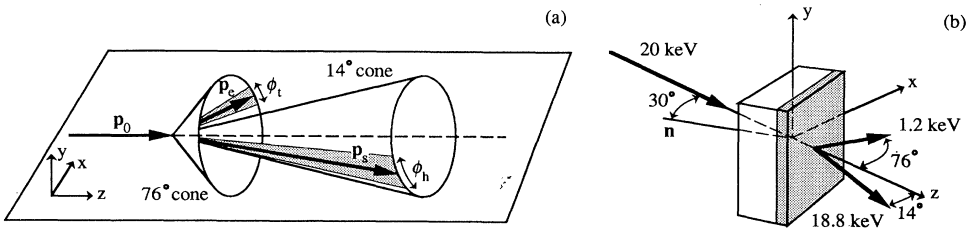

FIG. 3. A schematic representation of the noncoplanar asymmetric geometry used for the $(e, 2e)$ experiments. The kinematics chosen is such that the target electron momentum $\mathbf{q} = \mathbf{p}_s + \mathbf{p}_e - \mathbf{p}_0$ is along the y axis (a). The relative position of the target film with respect to the three electron beams is shown in (b), the shaded area indicating the overlayer.

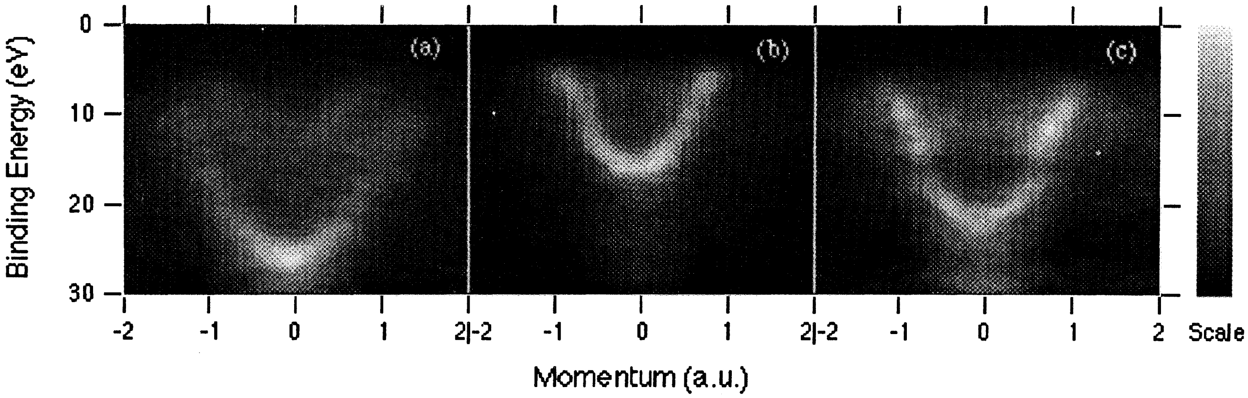

FIG. 4. The spectral momentum density of states, plotted in linear grey scale, for (a) the annealed amorphous carbon film, (b) the evaporated Si layer on the annealed C film, and (c) the polycrystalline SiC obtained from the Si/C film by annealing. Lighter shading represents stronger intensity. Binding energy is relative to the vacuum level of the spectrometer.

narrower in momentum and at lower binding energy. It becomes obvious that the centroid of the strong feature in the SiC data [Fig. 4(c)] falls in roughly the averaged position of the strong features in the C and Si data.

This relationship between the three spectral momentum densities can be understood from the one-electron-band theory of crystalline solids. In fact, the valence electronic structure of SiC can be described conceptually as a deviation from the diamond structure caused by the unequal potentials between the Si and the C sites. The symmetric part of the potential,

$$V_S(\mathbf{r}) = [V_{\rm Si}(\mathbf{r}) + V_{\rm C}(\mathbf{r})]/2, \tag{7}$$

determines the basic band structure of a hypothetical diamond-structure semiconductor, which should represent approximately the average of the band structure of diamond and silicon single crystals along each crystal orientation. The antisymmetric part of the potential can be defined as

$$V_A(\mathbf{r}) = [V_{\rm Si}(\mathbf{r}) - V_{\rm C}(\mathbf{r})]/2, \tag{8}$$

and it is the deviation of $V_A(\mathbf{r})$ from zero which distinguishes zinc-blende from diamond-structure semiconductors.[20] This concept can be used for all the zinc-blende and wurtzite structure semiconductors, although $V_A(\mathbf{r})$ becomes more complicated for the latter. One can therefore expect a smooth change of the many properties of the electronic structure depending on an ionicity factor based on $V_A(\mathbf{r})$ or a similar measure. One of the significant changes between the valence electronic structure of diamond structure semiconductors and that of zinc-blende or wurtzite structure semiconductors is that the bottom valence band splits off from the rest of the valence band to form the so-called antisymmetric gap in the latter. This antisymmetric gap of SiC is clearly visible at binding energies of about 16 eV (relative to the vacuum level of the spectrometer) and momenta of about 0.75 (a.u.), which corresponds to the averaged boundary of the first β-SiC Brillouin zone [Fig. 4(c)]. The spherical averaging due to the random orientation nature of the polycrystalline phase did not smear out this band gap.

Details of the results for the carbon and silicon are being published elsewhere. In the following, we will concentrate on the results for SiC. The experimental spectral momentum density $\rho(\epsilon, q)$ is firstly compared with theory in Fig. 5. Both densities are again presented as linear grey scale images, the lighter scale corresponding to a higher intensity. The theoretical density [Fig. 5(a)] has been convoluted using Gaussians of 2.0 eV and 0.15 a.u. full width at half maximum to account, respectively, for the finite energy and momentum resolution in the experiment. From here one can see that the major feature of the experimental density is reproduced rather well by the theoretical simulation, supporting the basic idea discussed in Sec. III.

Figure 5 presents only a qualitative comparison be-

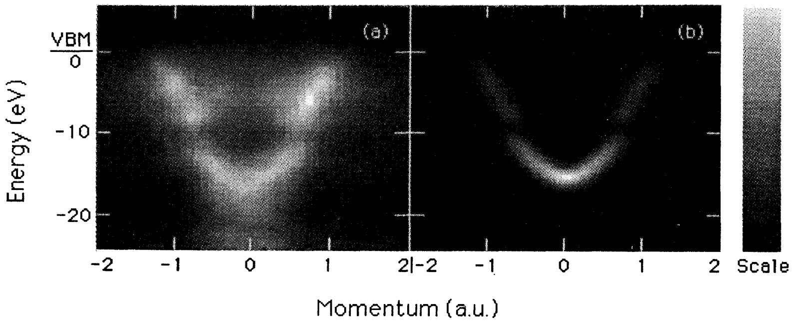

FIG. 5. The spectral momentum density of the polycrystalline SiC as measured in the $(e, 2e)$ experiment after an empirical deconvolution (a) and as calculated using the LMTO method (b). Intensity is plotted in linear grey scale. Lighter shading represents stronger intensity. Binding energy is relative to the valence-band maximum (VBM).

tween the experiment and the theory. To examine the quantitative agreement, one will need to study the details of these densities. For this purpose, we compare in Figs. 6 and 7, respectively, the energy profiles at selected momentum intervals and the momentum profiles at selected energy intervals of the experimental and theoretical spectral momentum densities. These two sets of profiles are complementary in understanding the quantitative aspects of these momentum densities. Let us first look at the energy profiles of Fig. 6. For each momentum, three different spectra are included: First, the markers with error bars are the raw data integrated over a momentum range of ±0.05 a.u. about the momentum value indicated. Second, the solid curves are results of an empirical deconvolution procedure taking into account mainly energy loss features due to plasmon excitation by one of the $(e,2e)$ electrons.[3] The primary purpose of the deconvolution is to remove the "background" at higher binding energies caused primarily by plasmon excitation, and to allow for an estimation of the area under the true coincidence peaks which gives the energy-integrated momentum density. Third, the dashed curves are the theoretical density shown in Fig. 5(b). The intensities are normalized uniformly according to the intensity of the main peak of the deconvoluted spectrum at $q = 0.05$ a.u. The energy axis is relative to the theoretical valence-band maximum (VBM), which is found at 7 eV below the vacuum level of the spectrometer for the present SiC data.

Two prominent features are clearly visible from Fig. 6, which can also be seen from Fig. 5(a), one dispersing upward from an energy of about −16 eV at zero momentum to an energy of −10 eV at a momentum of about 0.75 a.u., the intensity of which decreases rapidly beyond 0.85 a.u. The other prominent feature begins at a momentum of about 0.45 a.u. from an energy of −6 eV and continues towards higher momenta until it reaches an energy of about −1 eV at a momentum of about 1.25 a.u. They are identified as the lower and the upper valence bands of the polycrystalline SiC, respectively. The antisymmetric gap, with a width of about 3.5 eV, can be seen

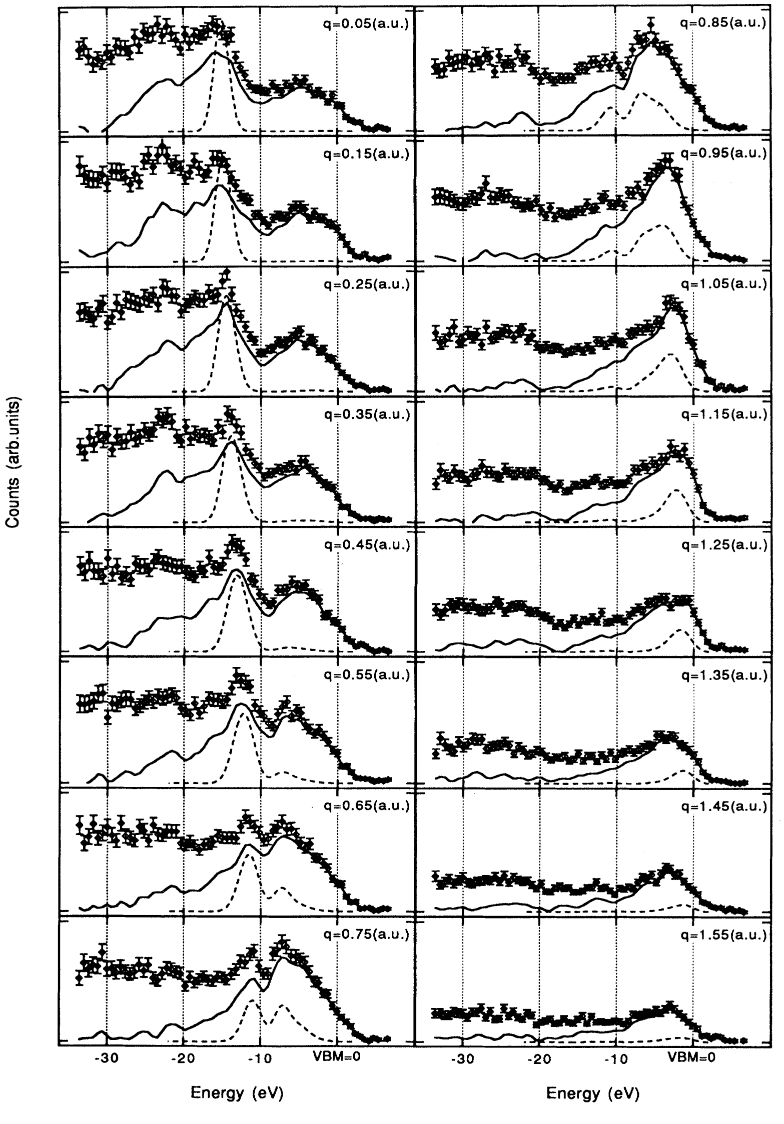

FIG. 6. The energy profiles of the SiC data for a series of momenta. The markers represent the raw data, solid curves are results after deconvoluting the energy loss background primarily due to plasmon excitation, and dashed curves are results from the LMTO calculation. Energy is relative to the valence-band maximum (VBM).

from the spectra for momentum values of 0.65–0.85 a.u. Obviously, the energy band dispersion represented by the peak positions of these two main features agrees very well with the theory.

With regard to the momentum densities, Fig. 6 has already presented a comprehensive picture. The line shape of the experimental momentum densities agrees reasonably well with the theory for momenta between 0.65 and 1.15 (a.u.), but is complicated for other momenta by two minor features present in the spectra, one appearing at energies of about -23 eV and the other at -5 eV. Both features appear dispersionless and are therefore unlikely to be satellites arising from plasmon excitation and electron correlation effects. Oxygen contamination is detected for the SiC sample using an *in situ* Auger spectrometer after the $(e,2e)$ experiment. The Auger spectrum is shown in Fig. 8. Since the sensitivity of the Auger spectrometer is not constant over the scanned range of the kinetic energy, information about the amount of oxygen contamination cannot be obtained from the relative intensity of the Auger signals. The relative intensity between the C(KLL) and the O(KLL) signals is, however, comparable to our earlier study on HOPG films directly after plasma etching (in an atmosphere of Ar and O_2 mixture),[9] in which we found considerable contributions from the oxygen at energies around -5 eV relative to the VBM. After the HOPG film was annealed to desorb the oxygen, the relative intensity compared to the main peak at -20 eV for zero momentum decreased by a factor of about 2.5. The majority of this change was expected to be due to the desorption of the oxygen contamination. X-ray photoemission spectroscopy (XPS) studies of the valence-band density of states of clean and oxygen exposed SiC(001) surfaces[21] also showed strong peaks at binding energies of about 23 and 6 eV below the VBM for the exposed surface. These energies match well with the energies of the two minor features in Fig. 6. We would therefore attribute these two minor features to oxygen contamination.

Without the presence of the oxygen contribution in

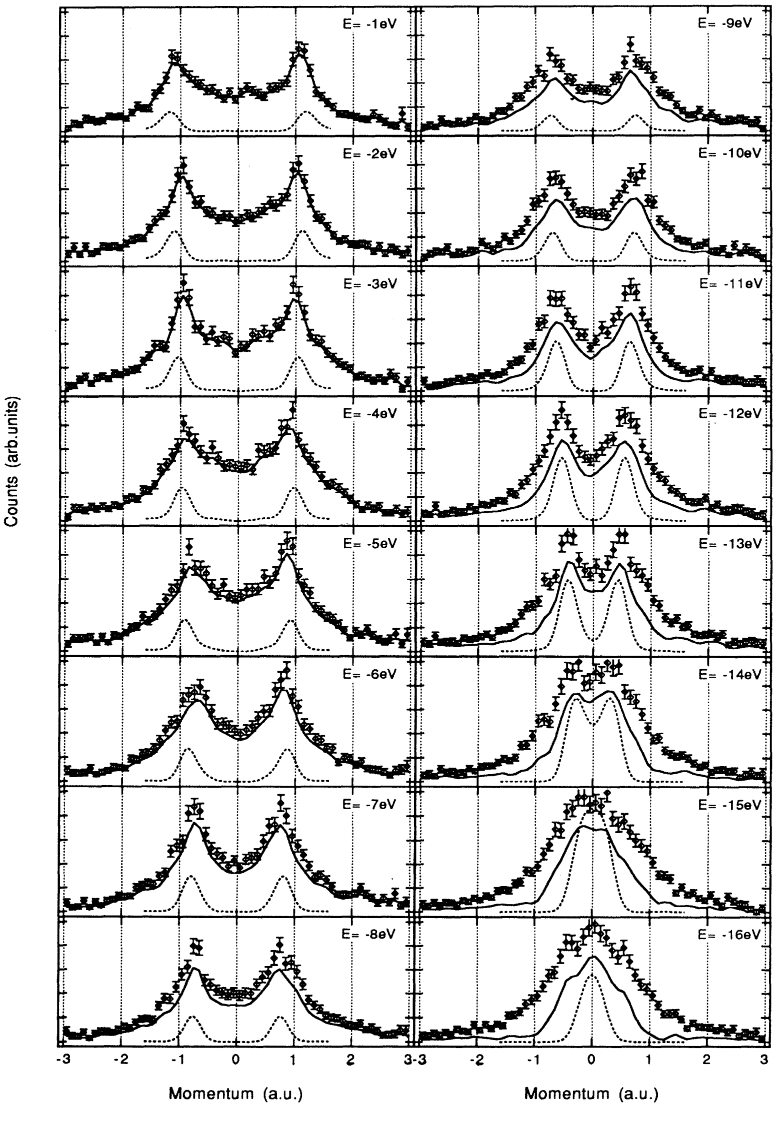

FIG. 7. The momentum profiles of the SiC data for a series of energies. The markers represent the raw data, solid curves are results after deconvoluting the energy loss background primarily due to plasmon excitation, and dashed curves are results from the LMTO calculation. Energies indicated are relative to the valence-band maximum (VBM).

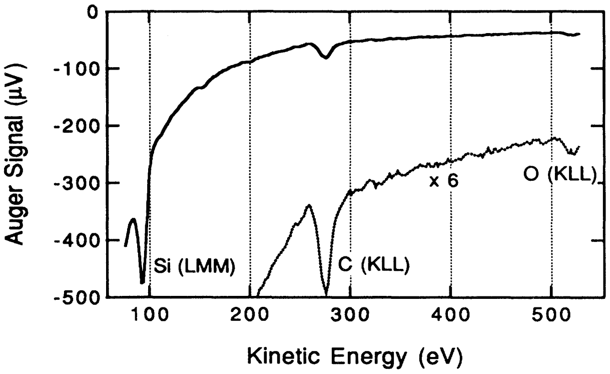

FIG. 8. Auger spectrum taken from the SiC thin film after the $(e,2e)$ measurement (solid curve). The dashed curve shows the C(KLL) and O(KLL) signal region enlarged by a factor of 6.

Fig. 6, the agreement between the experimental momentum density and the theoretical one would be expected to improve. But even after the removal of oxygen contribution, the width of the lower-energy dispersing structure is still considerably greater than that of the calculation. This could in part be due to electron correlation effects, leading to satellite structures. Comparisons with many-body calculations would be desirable here. Therefore, it remains to be seen how much improvement could be gained in an oxygen-"free" situation, and how adequate is our simple theoretical model in describing the experimental momentum density of this real disordered material.

We now return to the momentum profiles at selected energy intervals shown in Fig. 7. Only the profiles in the valence-band region are shown. Again three spectra are included for each energy value. The experimental ones (the markers and the solid curves) have been integrated for an energy range of ±0.5 eV around the energy values indicated. The theoretical curves (dashed curves) are normalized uniformly according to the intensity of the main peak at $E = -15$ eV, which is the bottom of the valence band. Unlike the energy profiles shown in Fig. 6, the line shape of the experimental profiles agrees rather well with the theory over most of the energy intervals presented. This is despite the fact that the experimental momentum profiles are much higher in intensity, particularly for energies closer to the VBM, than the theoretical ones as one may expect from the energy profiles shown in Fig. 6. The peak positions of both the experimental and the theoretical profiles again agree very well, but variations such as the antisymmetric gap may not be seen as easily from this type of plot. This type of plot is more useful when one is interested in the atomic orbital character of an energy level, such as in the case of atoms and molecules. Nevertheless, Fig. 7 shows that the lower valence band is predominantly s like and the upper valence bands are p like, indicating the constituent origin of the valence electrons.

To summarize the agreement between the experiment and the theoretical calculation, we present in Fig. 9 the comparison of the energy band dispersion (a) and the energy-integrated momentum density (b). The energy band dispersion is presented as if it was shown along with Fig. 5 to emphasize the similarity of the band image. One can see that the agreement is excellent. For the energy-integrated density, the area under the solid curves in Fig. 6 is used to estimate the experimental points. The trend of the experimental density is reproduced reasonably well by the theory, although the experiment gives significantly enhanced density at high momenta. This can also be seen by comparing the theoretical and experimental plots in Fig. 5.

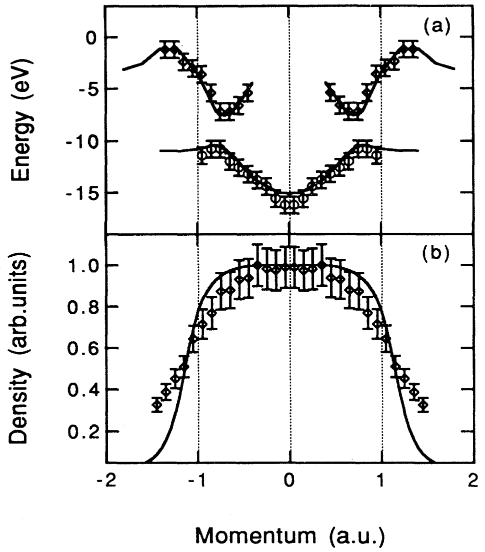

FIG. 9. Comparison of the energy band dispersion (a) and the energy-integrated momentum density (b) between experiment (markers) and the LMTO calculation (solid curves). Energy is relative to the valence-band maximum (VBM).

V. CONCLUSION

In conclusion, the imaging capacity of the $(e,2e)$ technique for the spectral momentum density of solid materials is demonstrated. The relationship between the spectral momentum densities of amorphous carbon, amorphous silicon, and silicon carbide is well described by the one-electron-band theory of crystalline solids. For the polycrystalline silicon carbide, the band structure is represented well by the spherically averaged LMTO calculation. However, towards a quantitative agreement for the momentum density further work is still required. For example, the difference between the local order of the disordered material and that of the corresponding crystalline form has been neglected in the calculation. Surface effects, which may be important under the present experimental kinematics, have also not been taken into account. There might also be fine details in the electronic structure of amorphous and polycrystalline solids which cannot be resolved under the present energy and momentum resolutions. Hopefully, improving the energy and momentum resolutions will make this possible in the future.

ACKNOWLEDGMENTS

This work has been supported by the Australian Research Council. The authors are grateful for the skillful support of the technical staff of the ESM Centre.

---

[*] Present address: Research School of Physical Sciences and Engineering, Australian National University, Canberra, ACT 2601, Australia.

[1] I. E. McCarthy and E. Weigold, Rep. Prog. Phys. **51**, 299 (1988); **54**, 789 (1991).

[2] V. G. Levin, V. G. Neudatchin, and Yu. F. Smirnov, Phys. Status Solidi **49**, 489 (1972).

[3] R. Jones and A. L. Ritter, J. Electron Spectrosc. Relat. Phenom. **40**, 285 (1986).

[4] U. Amaldi, Jr., A. Egidi, R. Marconero, and G. Pizzella, Rev. Sci. Instrum. **40**, 1001 (1969).

[5] A. L. Ritter, J. R. Dennison, and R. Jones, Phys. Rev. Lett. **53**, 2054 (1984).

[6] C. Gao, A. L. Ritter, J. R. Dennison, and N. A. W. Holzwarth, Phys. Rev. B **37**, 3914 (1988).

[7] P. Hayes, M. A. Bennett, J. Flexman, and J. F. Williams, Phys. Rev. B **38**, 13371 (1988).

[8] P. Storer, R. S. Caprari, S. A. C. Clark, M. Vos, and E. Weigold, Rev. Sci. Instrum. **65**, 2214 (1994).

[9] M. Vos, P. Storer, S. Canney, A. S. Kheifets, I. E. McCarthy, and E. Weigold, Phys. Rev. B **50**, 5635 (1994).

[10] M. Vos, P. Storer, Y. Q. Cai, I. E. McCarthy, and E. Weigold, Phys. Rev. B **51**, 1866 (1995).

[11] M. Vos, P. Storer, Y. Q. Cai, A. S. Kheifets, I. E. McCarthy, and E. Weigold, J. Phys.: Condens. Matter (to be published).

[12] J. Robertson, Adv. Phys. **32**, 361 (1983).

[13] J. M. Ziman, J. Phys. C **4**, 3129 (1971).

[14] J. Keller, J. Phys. C **4**, 3143 (1971).

[15] R. F. Davis, Physica B **185**, 1 (1993).

[16] A. R. Verma and P. Krishna, *Polymorphism and Polytypism in Crystals* (Wiley, New York, 1966), Chap. 5.

[17] H. L. Skriver, *The LMTO Method* (Springer-Verlag, New York, 1984).

[18] A. S. Kheifets, J. Lower, K. J. Nygaard, S. Utteridge, M. Vos, E. Weigold, and A. L. Ritter, Phys. Rev. B **49**, 2113 (1994).

[19] H. Inui, H. Mori, A. Suzuki, and H. Fujita, Philos. Mag. B **65**, 1 (1992), and references therein.

[20] M. L. Cohen and J. R. Chelikowsky, *Electronic Structure and Optical Properties of Semiconductors* (Springer-Verlag, Berlin, 1988).

[21] V. M. Bermudez, J. Appl. Phys. **66**, 6084 (1989).

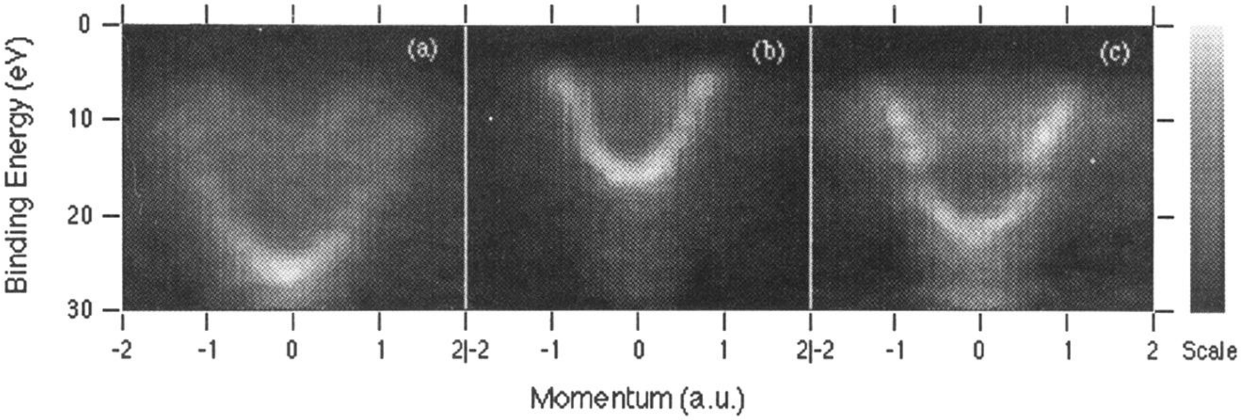

FIG. 4. The spectral momentum density of states, plotted in linear grey scale, for (a) the annealed amorphous carbon film, (b) the evaporated Si layer on the annealed C film, and (c) the polycrystalline SiC obtained from the Si/C film by annealing. Lighter shading represents stronger intensity. Binding energy is relative to the vacuum level of the spectrometer.

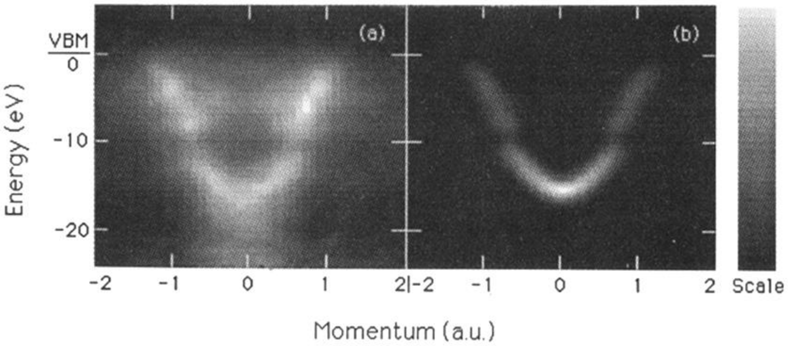

FIG. 5. The spectral momentum density of the polycrystalline SiC as measured in the $(e, 2e)$ experiment after an empirical deconvolution (a) and as calculated using the LMTO method (b). Intensity is plotted in linear grey scale. Lighter shading represents stronger intensity. Binding energy is relative to the valence-band maximum (VBM).